Determining and modelling a complete time-temperature-transformation diagram for a Pt-based metallic glass former through combination of conventional and fast scanning calorimetry

M. Frey [a,*], N. Neuber [a], M. Müller [a], O. Gross [b], S.S. Riegler [a], I. Gallino [a], R. Busch [a]

[a] *Chair of Metallic Materials, Saarland University, Campus C6.3, Saarbrücken 66123, Germany*
[b] *Amorphous Metal Solutions GmbH, Michelinstraße 9, Homburg 66424, Germany*

ABSTRACT

State of the art fast differential scanning calorimetry (FDSC) is used to complement conventional differential scanning calorimetry (DSC) studies about the isothermal time-temperature-transformation (TTT) diagram of the bulk metallic glass forming liquid $Pt_{42.5}Cu_{27}Ni_{9.5}P_{21}$ to allow a comprehensive study of the crystallization kinetics of this system over a broad temperature range. FDSC and DSC data align well in the low-temperature region of the crystallization nose but show distinct discrepancies in the high-temperature region as the FDSC studies reveal faster crystallization times. The results are mathematically described and discussed based on the Johnson-Mehl-Avrami-Kolmogorov (JMAK) equation. Thereby, either homogeneous or heterogeneous nucleation is assumed, depending on the respective experimental conditions in FDSC and DSC studies. With this approach, the complete TTT diagram can be modelled as superposition of two sequential JMAK fits.

$Pt_{42.5}Cu_{27}Ni_{9.5}P_{21}$ is a well-known bulk metallic glass forming system that features advanced glass forming ability (GFA) with a critical diameter d_c of 20 mm [1], which is one of the best GFA found in the whole alloy system. The alloy has been subject to intense research in our group [2–6] as it differs significantly from other bulk glass-forming compositions. Within the Pt-P-based bulk glass-forming liquids developed by Schroers and Johnson [1], the $Pt_{42.5}Cu_{27}Ni_{9.5}P_{21}$ is the kinetically strongest liquid [2,3]. Additionally, only the total structure factor of the $Pt_{42.5}Cu_{27}Ni_{9.5}P_{21}$ liquid exhibits a prominent pre-peak at low scattering vectors [2,4], which is interpreted as the signature of a pronounced medium-range order that evolves upon undercooling [4,5]. Moreover, the description of the experimentally determined time-temperature-transformation (TTT) diagram with the classical nucleation theory yields a relatively high value of the interfacial energy of 0.11 J/m^2 ± 0.01 J/m^2. This is considered as a key parameter explaining the high GFA of the Pt-P-based liquids despite their fragile kinetics and the relatively high driving force for crystallization, e.g. compared to Pd-P based liquids [5,6]. The previous crystallization experiments were performed in a conventional DSC, allowing only limited heating and cooling rates, prohibiting an experimental determination of the minimum crystallization time (tip of the crystallization nose). Thus, it was determined from the fit of the low- and high-temperature crystallization data. The recent developments in the field of fast differential scanning calorimetry (FDSC) now offer, for the first time, the possibility to collect crystallization data of many bulk glass-forming liquids at the tip of the crystallization nose. While the commercially available Mettler-Toledo FDSC 1 is only able to measure the TTT-diagram of glass-forming liquids with liquidus temperatures below 793 K (e.g. Au-based compositions [7,8]), the latest version, the FDSC 2+, can achieve temperatures up to 1273 K [9], giving access to a broad field of different alloy systems. Therefore, the authors chose the $Pt_{42.5}Cu_{27}Ni_{9.5}P_{21}$ bulk glass-forming system as a model system to verify the predictions of our previous study by closing the data-gap between high and low temperatures and to identify the influence of the different experimental conditions in the FDSC 2+ on the crystallization process.

The FDSC studies were performed using a Mettler-Toledo FDSC2+ equipped with a MultiSTAR UFH 1 high-temperature chip sensor with silicon nitride (Si_3N_4) surface, allowing for maximum temperatures up to 1273 K [9]. To provide fast cooling rates, a Huber HC100 intracooler was used to hold the sensor support temperature at 188 K. High-purity argon gas flow of 60 ml/min was used to prevent oxidation effects. Two samples were subsequently measured on two different chip sensors for improved statistics. Each sample was cut from the same melt spun ribbon and placed on the respective sensor area, followed by melting via

---

* Corresponding author.
  E-mail address: maximilian.frey@uni-saarland.de (M. Frey).

several heating scans to temperatures above T_l to obtain good and stable thermal contact between sample and sensor. Measuring the enthalpy of melting upon heating and comparing it to the literature value [2] allows to estimate the sample masses to be roughly 430 ng and 350 ng, respectively [10,11]. These relatively high masses are chosen to avoid sample size effects on the thermal stability [10,12]. Prior to each isothermal measurement, the sample was equilibrated at 973 K (about 100 K above T_l) for several seconds, followed by fast cooling to the respective temperature of isothermal measurement with 10,000 K/s. Every isothermal temperature step was measured at least three times. The inset in Fig. 1 exemplarily depicts a typical heat flow signal obtained at 703 K. The exothermal crystallization event was integrated to obtain the times at which 1%, 50%, and 99% of the heat release has occurred (dashed line). All averaged data points corresponding to these percentage-values are shown in the main window of Fig. 1, thereby forming a typical crystallization nose shape. The standard deviations are given as error bars. At lower temperatures below 613 K, the measurement window is limited by the small sample mass, as the growth-controlled crystallization event smears out over long timescales, thereby getting undetectable due to the deteriorated signal-to-noise ratio [7,13]. At elevated temperatures above 763 K, the nucleation-controlled crystallization event exhibits the trend to shift to longer timescales, exceeding the time limit for data acquisition [7].

The low-temperature (LT) and high-temperature (HT) DSC measurements previously published in [6] were performed using a conventional Perkin-Elmer DSC 8500. For LT-DSC measurements, as-cast bulk samples were heated in aluminum pans with 2 K/s from the glassy state to the respective isotherm above T_g under high-purity argon flow. HT-measurements were performed by equilibrating the alloy in the equilibrium liquid state at the maximum operation temperature of the device of 973 K (about 100 K above the liquidus temperature of 874 K) and subsequent cooling to the respective measurement temperature below T_m with 2 K/s. The samples were measured under high-purity argon flow in graphite pans and embedded in molten B_2O_3 flux. Several HT-measurements were performed for each temperature. Fig. 2 combines the FDSC data of this work with the DSC data from [6]. In order to harmonize the appearance of the TTT diagram, the original HT-DSC datapoints [6] are averaged for each respective temperature step. Standard deviations in form of error bars are only shown for 1% data points to assure the clarity of the plot. While LT-DSC and low-temperature FDSC data align quite well, a distinct mismatch in timescales is found between the HT-DSC data and the overlapping high-temperature FDSC data, as the latter shows relatively short crystallization times. To further quantify this offset, the Johnson-Mehl-Avrami-Kolmogorov (JMAK) equation is used [14–18]. This mathematical approach based on classical nucleation theory describes the temperature dependency of steady state crystallization kinetics and can be utilized to model the crystallization nose in a TTT diagram. At a given temperature, the time t(T) until a portion x of the undercooled liquid is crystallized is calculated as

$$t(T) = \left(-\frac{3 \ln(1-x)}{\pi\, I(T)\, u(T)^3} \right)^{1/4}. \tag{1}$$

The homogeneous nucleation rate $I_{hom}(T)$ and the crystal growth rate $u(T)$ are determined as:

$$I_{hom}(T) = \frac{A_\nu}{\eta(T)}\, exp\left(-\frac{16\,\pi}{3\,k_B\,T}\, \frac{\gamma^3}{\Delta g_{l-x}(T)^2} \right), \tag{2}$$
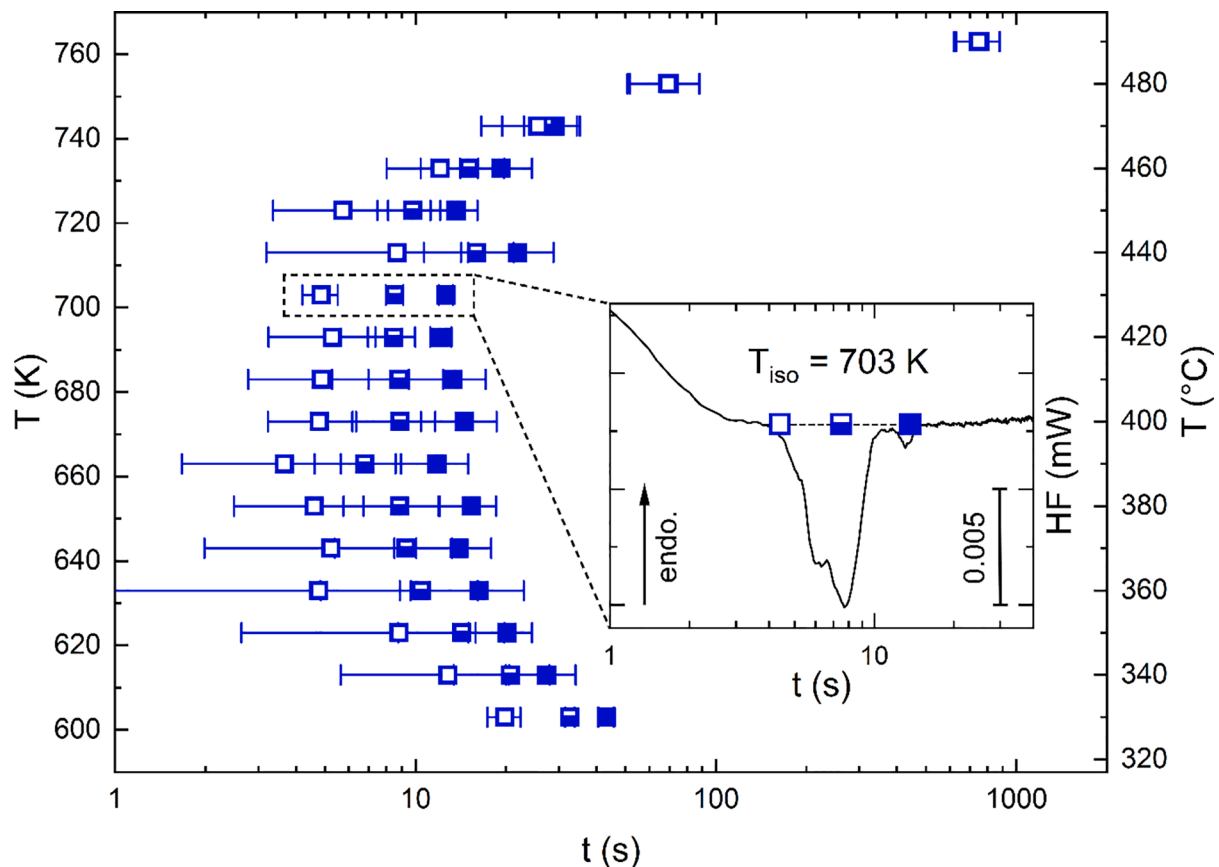
Fig. 1. Results of isothermal FDSC crystallization studies. The inset shows an exemplary measurement at 703 K. In the main window, averaged crystallization times for 1% (open squares), 50% (half-filled squares), and 99% (filled squares) of the occurred crystallization enthalpy are displayed. The standard deviations are given as error bars.
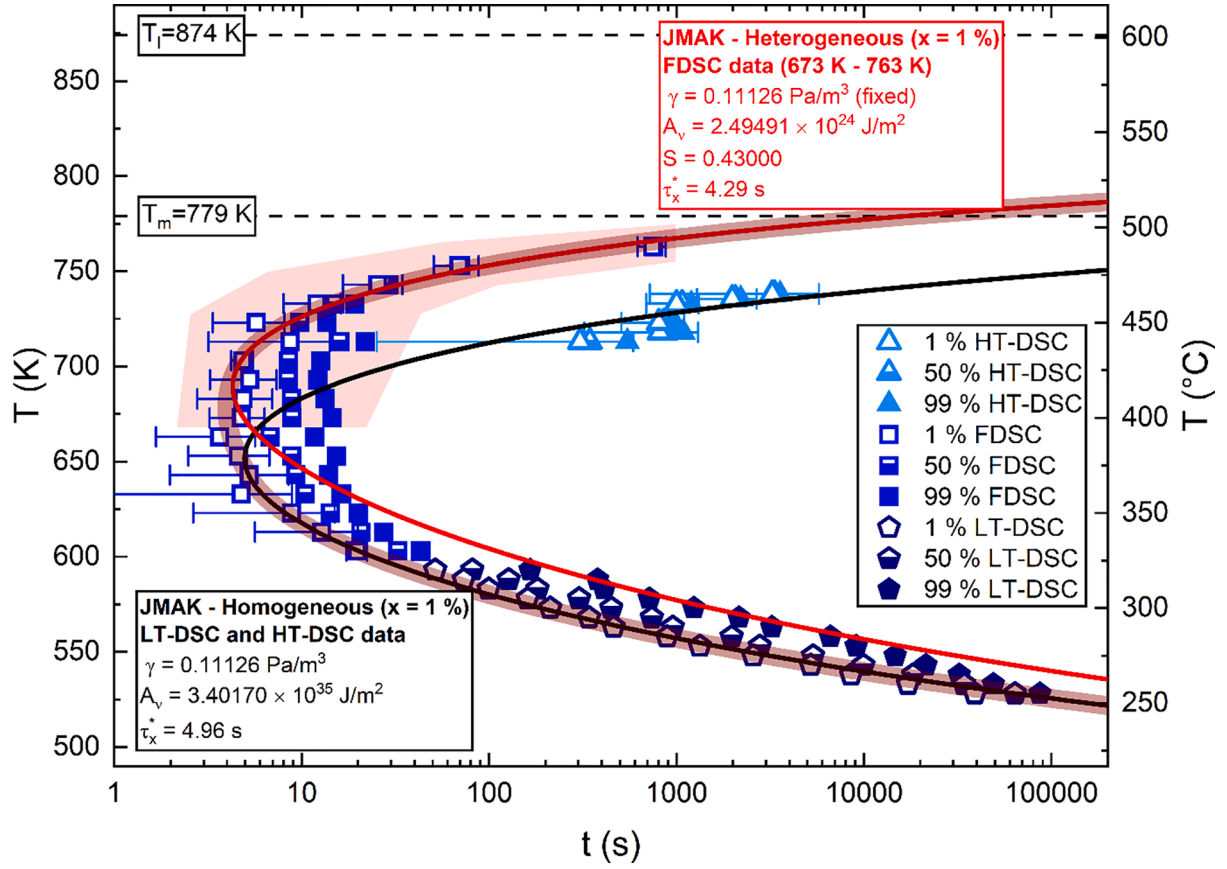
Fig. 2. Complete isothermal TTT diagram of the $Pt_{42.5}Cu_{27}Ni_{9.5}P_{21}$ alloy consisting of LT-DSC [6], HT-DSC [6], and FDSC crystallization data. Until about 668 K (below the transparent red area), LT-DSC and FDSC results show good alignment. In contrast, HT-DSC data and high-temperature FDSC data show drastic disagreement, the FDSC studies reveal crystallization times about two orders of magnitude faster than the HT-DSC data. This discrepancy is underlined by the JMAK fit of the LT- and HT-DSC data that assumes homogeneous crystallization (black solid line). Using the modification for heterogeneous crystallization, the red solid line indicates the JMAK fit of the FDSC data above 668 K (transparent red area), allowing to mathematically describe the upper FDSC crystallization nose. Consequently, the combined data set of FDSC and LT-DSC can be modeled by a superposition of both JMAK fits, as indicated by the broad transparent line (For interpretation of the references to color in this figure legend, the reader is referred to the web version of this article).

$$u(T) = \frac{k_B}{3 \, \pi \, a_0^2} \, \frac{T}{\eta(T)} \, \left(1 - exp\left(\frac{n}{k_B} \, \frac{\Delta g_{l-x}(T)}{T}\right)\right) \tag{3}$$

with a preexponential factor A_ν, the volume-specific free energy difference between liquid and crystalline state $\Delta g_{l-x}(T)$, the interfacial energy between liquid and crystalline state γ, the average atomic diameter a_0, the average atomic volume n, and the temperature-dependent equilibrium viscosity $\eta(T)$. $\Delta g_{l-x}(T)$ is calculated from molar heat capacity data $\Delta C_{p,l-x}(T)$, density ρ, molar mass M, as well as the molar values of enthalpy and entropy of fusion, ΔH_f and ΔS_f [19] as

with the high-temperature limit of viscosity η_0, the fragility parameter D* and the VFT-temperature T_0 published in [2,3]. Most of the applied thermodynamic and kinetic parameters in these equations are empirically defined and are taken from [2,3,6], as listed in Table 1 (the parameters a, b, c, and d are the fitting parameters used to model the heat capacity as described in e.g. [21]). Only A_ν and γ are left as free fitting parameters. Here, it should be noted that the heat capacity data used for calculations represents the equilibrium crystalline mixture, which does not necessarily reflect the thermodynamic conditions of initial nucleation but serves as a lower estimate of the actual driving force for crystallization of the primary phase.

$$\Delta g_{l-x}(T) = \frac{\rho}{M} \Delta G_{l-x}(T) = \frac{\rho}{M} \left(\Delta H_f + \int_{T_l}^{T} \Delta C_{p,l-x}(T') \, dT' - T \left(\Delta S_f + \int_{T_l}^{T} \frac{\Delta C_{p,l-x}(T')}{T} \, dT'\right)\right). \tag{4}$$

The viscosity data is described by the Vogel-Fulcher-Tammann (VFT) equation [20] as

$$\eta(T) = \eta_0 \, exp\left(\frac{D^* \, T_0}{T - T_0}\right), \tag{5}$$

In a first step, the JMAK equation with assumed homogeneous crystallization is used to explicitly fit the LT- and HT-DSC data without taking FDSC results into account, in analogy to the fitting procedure in [6]. For a crystalline fraction of $x = 0.01$ (open symbols), an A_ν value of 3.40170×10^{35} Pa/m^3 and a γ value of 0.11126 J/m^2 are provided. These parameters are almost identical to the ones published in [6], only

Table 1

JMAK parameters provided by empirically studies and through fitting procedure.

Thermodynamic parameters taken from [2,6]	
a	9.61384×10^{-3} J/(g-atom K^2)
b	5.52829×10^6 J K/g-atom
c	-6.14630×10^{-3} J/(g-atom K^2)
d	1.64663×10^{-5} J/(g-atom K^3)
T_l	874 K
ΔH_f	10.5 J/g-atom
ΔS_f	12.01 J/(g-atom K)
Kinetic parameters taken from [2,3]	
η_0	4×10^{-5} Pa s
D*	15.3
T_0	354.4 K
JMAK fit of DSC data (homogeneous nucleation assumed)	
A_ν	3.40170×10^{35} Pa/m^3
γ	0.11126 ± 0.00092 J/m^2
τ_x^*	4.96 s
d_c (calculated from τ_x^*)	16.2 mm
JMAK fit of FDSC data (heterogeneous nucleation assumed, 673 K–763 K)	
A_ν	2.49491×10^{24} Pa/m^3
γ	0.11126 J/m^2 (fixed)
$S(\theta)$	0.43000 ± 0.01838
Θ	$84.6° \pm 1.4°$
τ_x^*	4.29 s
d_c (calculated from τ_x^*)	15.3 mm

slight deviations arise from the fact that the HT-DSC data was not averaged for fitting in the original article. The corresponding fit curve is displayed in Fig. 2 as a black solid line. The minimal crystallization time given by the fit curve, the so-called nose time τ_x^*, is 4.96 s. Johnson et al. [22] derived an empirical equation that connects the crystallization nose time τ_x^* with the critical casting diameter d_c (in mm) as

$$\tau_x^* = 0.00419 \, (d_c)^{2.54}. \tag{6}$$

Accordingly, the nose time interpolated by the DSC JMAK fit would correspond to a d_c value of 16.2 mm. This is in reasonable agreement with the experimentally confirmed d_c of 20 mm [1]. These samples were produced by water quenching the equilibrium liquid under a protective environment of B_2O_3 flux in a quartz tube. The use of a fluxing agent drastically reduces the probability of heterogeneous nucleation, as it purifies the melt from oxidic contaminations and shields it to some degree from external nucleation sites [6,8,23,24]. The HT-DSC measurements mimic these conditions since the studied sample is also submerged in a B_2O_3 flux, thereby decreasing the probability of interfering reactions with gaseous impurities or the crucible pan. Indeed, the large scatter in HT-DSC crystallization times (see error bars in Fig. 2) speaks for the typical stochastic nature of a crystallization process controlled by (homogeneous) nucleation at these elevated temperatures. Thus, albeit heterogeneous nucleation cannot be completely excluded, it seems to play no major role in the crystallization behavior of the HT-DSC measurements. In case of the LT-DSC studies, the beneficial influence of a fluxing agent is absent, yet, the critical nuclei size at such low temperatures is already very small, so that the liquid does not lack on overcritical nuclei. Instead, the crystallization times are mainly dominated by the sluggish kinetics. Hence, the influence of the nucleation rate, and therefore of heterogeneous nucleation effects, on the crystallization kinetics becomes less pronounced at these low temperatures. The crystallization is rather growth-controlled as pointed out in numerous studies [6,8,13,24]. This leads to reproducible crystallization times with crystallization events stretched over large time spans, as demonstrated by the LT-DSC data in Fig. 2. Based on these considerations, two assumptions are made. First, it seems reasonable that heterogeneous nucleation plays no crucial role for the observed crystallization kinetics of all the DSC data, leaving the assumption of homogeneous nucleation for JMAK fitting as a valid approach. Second, it is assumed that DSC data and the resulting JMAK fit correspond

relatively well to the crystallization conditions present for the fluxed and quenched samples reported in [1].

Comparing DSC-JMAK fit and FDSC data, excellent agreement is found in the low temperature part of the crystallization nose, but deviations increase for temperatures above the nose tip (above about 668 K), indicated by the transparent red area in Fig. 2. This trend finds its climax in the FDSC data at the highest temperatures, where crystallization events occur about two orders of magnitude faster than in HT-DSC measurements under fluxing conditions. DSC-based isothermal TTT studies on a Pd-based bulk metallic glass former [25] reported a quite similar behavior by comparing the crystallization times of fluxed and unfluxed samples. While no strong discrepancy was found in the low-temperature regime, the unfluxed samples showed distinctly shorter crystallization times in the high-temperature region above the tip of the crystallization nose, which was addressed to heterogeneous nucleation effects on the sample surface. For the present FDSC studies, the sample is molten directly on the UFH 1 sensor to form a rigid connection that permits fast temperature changes, but also increases the possibility of heterogeneous nucleation on the silicon nitride surface of the sensor.

With these aspects in mind, modifications that take heterogeneous nucleation effects into account might provide a more suitable approach for JMAK fitting of the FDSC crystallization nose. In case of heterogeneous nucleation, the free energy barrier to form a critical nucleus is gradually reduced, which can be mathematically expressed by a shape factor $S(\theta)$ included for the heterogeneous nucleation rate $I_{het}(T)$ [26]:

$$I_{het}(T) = \frac{A_\nu}{\eta(T)} \, exp\left(-S(\theta) \, \frac{16 \, \pi}{3 \, k_B \, T} \, \frac{\gamma^3}{\Delta g_{l-x}(T)^2} \right), \tag{7}$$

where $S(\theta)$ formally corresponds to a wetting angle θ between the formed nucleus and the substrate surface [26] as

$$S(\theta) = \frac{1}{4} \, (2 + cos(\theta)) \, (1 - cos(\theta))^2. \tag{8}$$

This modified JMAK equation now features three fitting parameter A_ν, γ, and $S(\theta)$, instead of two. One of them must be fixed to avoid an overparameterization of the fit. To solve this apparent problem, we assume in the following that for LT-, HT-DSC, and FDSC data, the very same primary crystalline phase nucleates. Only in the nucleation-controlled high-temperature region of the FDSC data set, the crystallization kinetics accelerate due to the mentioned experimental conditions and the resulting increased effect of heterogeneous nucleation. With this approach, the interfacial energy can be fixed to the value found for the homogeneous DSC JMAK fit (0.11126 J/m^2).

In a first attempt, the heterogeneous JMAK fit fails to provide satisfying results for the combined LT-DSC and FDSC data ($x = 0.01$). The fit massively underestimates the nose time, visible in the orange solid line in Fig. A in the Supplementary Information. Similar problems evolve when only the FDSC data is fitted this way (brown dashed line). Here, the JMAK fit fails to describe the rather blunt shape of the FDSC crystallization nose data, since the whole set of empirically given thermodynamic and kinetic parameters predetermines a relatively sharp and narrow nose geometry [5]. To avoid this, only the FDSC data ($x = 0.01$) that deviates from the course of the homogeneous DSC JMAK fit is fitted, i.e. for temperatures above 668 K (the FDSC data in the transparent red area). This fit (red solid line in Fig. 2) allows a good mathematical description of the upper part of the FDSC crystallization nose and provides a $S(\theta)$ value of 0.43000, which formally corresponds, according to Eq. (8), to a wetting angle θ of 84.6°, a reasonable value for heterogeneous nucleation processes [27–29]. Geometrically, this would imply an almost half-spherical crystalline nucleus that forms onto the surface of the heterogeneous nucleation site. Albeit the nose tip of heterogeneous FDSC JMAK fit is about 50 K higher than for the homogeneous DSC JMAK fit, the nose time remains with 4.29 s basically unchanged and corresponds, according to Eq. (6), to a d_c of 15.3 mm. So, while the thermal stability in the high-temperature region of the FDSC

crystallization nose is distinctly affected, the GFA, defined by τ_x^* and the resulting critical cooling rate and critical diameter, remains almost un-affected. This is a promising result for industry-relevant processing routes of $Pt_{42.5}Cu_{27}Ni_{9.5}P_{21}$, where rather suboptimal conditions (no fluxing, shear flow) are present, e.g. in case of die casting or suction casting processes. Still, it should be considered that the impact of het-erogeneous nucleation quantified in this work is only valid for the pre-sent setup and can change massively under different conditions.

In summary, the use of the FDSC 2+ allows to bridge the gap in the TTT diagram between LT- and HT-DSC and to directly observe the ki-netics at the crystallization nose. In the upper part of the FDSC crys-tallization nose, crystallization timescales decouple from the HT-DSC results and show distinctly shorter crystallization times. This is traced back to the absence of a fluxing agent in case of the FDSC setup, leaving the alloy prone to increased heterogeneous crystallization effects that catalyze crystallization. The JMAK equation is used to sequentially model crystallization kinetics under homogeneous and heterogeneous nucleation conditions with satisfying agreement. Combined LT-DSC and HT-DSC data can be well described using a single homogeneous JMAK fit, as the fluxing conditions of HT-DSC measurements effectively frus-trate heterogeneous nucleation at elevated temperatures. In case of an unfluxed sample environment, where heterogeneous nucleation effects gain influence with rising temperature, the combined FDSC and LT-DSC data set can be modeled through a superposition of homogeneous JMAK fitting at low temperatures and heterogeneous JMAK fitting for higher temperatures above the crystallization nose, as indicated by the broad transparent line in Fig. 2. To our knowledge, this is the first time such a combination of homogeneous and heterogeneous JMAK fitting is used to describe the isothermal crystallization behavior of a metallic glass former. This approach allows to obtain geometrical information about the heterogeneously formed nucleus in terms of the calculated wetting angle θ of 84.6°. Assuming that the heterogeneous nucleation occurs in the sample sensor interface, the present study could be seen as a starting point for a systematic study on different sensor materials (or sensor surface coatings) and their influence on heterogeneous nucleation ef-fects. Due to the extensive amount of accessible data, the $Pt_{42.5}Cu_{27}$-$Ni_{9.5}P_{21}$ alloy would make a good model system, here. Such extensive studies would further benefit from imaging methods like SEM or TEM to verify the used assumption that the same primary crystalline phase forms in case of homogeneous and heterogeneous nucleation.

Moreover, another valuable approach would be a systematic study of the effect of changed overheating in the equilibrium liquid state on the crystallization kinetics of $Pt_{42.5}Cu_{27}Ni_{9.5}P_{21}$, as encouraged by earlier works [6,30].

Declaration of Competing Interest

The authors declare that they have no known competing financial interests or personal relationships that could have appeared to influence the work reported in this paper.

Supplementary materials

Supplementary material associated with this article can be found, in the online version, at doi:10.1016/j.scriptamat.2022.114710.

References

[1] J. Schroers, W.L. Johnson, Appl. Phys. Lett. 84 (2004) 3666–3668.
[2] O. Gross, B. Bochtler, M. Stolpe, S. Hechler, W. Hembree, R. Busch, I. Gallino, Acta Mater. 132 (2017) 118–127.
[3] M. Frey, N. Neuber, O. Gross, B. Zimmer, W. Possart, R. Busch, J. Phys. Condens. Matter 32 (2020) 1–9.
[4] O. Gross, N. Neuber, A. Kuball, B. Bochtler, S. Hechler, M. Frey, R. Busch, Commun. Phys. 2 (2019) 83.
[5] O. Gross, Precious Metal Based Bulk Glass-Forming Liquids: Development, Thermodynamics, Kinetics and Structure, Saarland University, 2018.
[6] O. Gross, S.S. Riegler, M. Stolpe, B. Bochtler, A. Kuball, S. Hechler, R. Busch, I. Gallino, Acta Mater. 141 (2017) 109–119.
[7] N. Neuber, M. Frey, O. Gross, J. Baller, I. Gallino, R. Busch, J. Phys. Condens. Matter (2020) 1–8.
[8] S. Pogatscher, P.J. Uggowitzer, Appl. Phys. Lett. 104 (2014) 1–5.
[9] O. Haruyama, T. Makimura, T. Miyakawa, K. Sugiyama, High Temp. Mater. Process. 29 (2010) 381–392.
[10] S. Pogatscher, D. Leutenegger, A. Hagmann, P.J. Uggowitzer, J.F. Löffler, Thermochim. Acta 603 (2015) 46–52.
[11] J.Q. Wang, Y. Shen, J.H. Perepezko, M.D. Ediger, Acta Mater. 104 (2016) 25–32.
[12] N. Sohrabi, J.E.K. Schawe, J. Jhabvala, J.F. Löffler, R.E. Logé, Scr. Mater. 199 (2021), 113861.
[13] C. Wrana, J.E.K. Schawe, Thermochim. Acta 690 (2020).
[14] A.N. Kolmogoroff, Izv. Akad. Nauk SSSR. Seriya Mat. 1 (1937) 355–359.
[15] M. Avrami, J. Chem. Phys. 7 (1939) 1103–1112.
[16] M. Avrami, J. Chem. Phys. 8 (1940) 212–224.
[17] M. Avrami, J. Chem. Phys. 9 (1941) 177–184.
[18] J.W. Christian, The Theory of Transformations in Metals and Alloys, Elsevier Ltd., 2002.
[19] I. Gallino, J. Schroers, R. Busch, J. Appl. Phys. 108 (2010).
[20] C.A. Angell, Science 267 (1995) 1924–1935 (80-.).
[21] M. Frey, R. Busch, W. Possart, I. Gallino, Acta Mater. 155 (2018) 117–127.
[22] W.L. Johnson, J.H. Na, M.D. Demetriou, Nat. Commun. 7 (2016).
[23] H.W. Kui, A.L. Greer, D. Turnbull, Appl. Phys. Lett. 45 (1984) 615–616.
[24] J. Schroers, Y. Wu, R. Busch, W.L. Johnson, Acta Mater. 49 (2001) 2773–2781.
[25] J. Schroers, Y. Wu, W.L. Johnson, Philos. Mag. A 82 (2002) 1207–1217.
[26] D.A. Porter, K.E. Easterling, Phase Transformations in Metals and Alloys, Chapman & Hall, 1992.
[27] D. Turnbull, J. Chem. Phys. 20 (1952) 411–424.
[28] K.L. Moazed, J.P. Hirth, Surf. Sci. 3 (1965) 49–61.
[29] S. Krüger, J. Deubener, Front. Mater. 3 (2016) 1–9.
[30] S. Mukherjee, Z. Zhou, J. Schroers, W.L. Johnson, W.K. Rhim, Appl. Phys. Lett. 84 (2004) 5010–5012.